NANO LETTERS
Cite This: Nano Lett. 2019, 19, 1104−1111
Letter
pubs.acs.org/NanoLett

Dense Electron−Hole Plasma Formation and Ultralong Charge Lifetime in Monolayer MoS_2 via Material Tuning

Alexander W. Bataller,[†] Robert A. Younts,[†] Avinash Rustagi,[†] Yiling Yu,[‡] Hossein Ardekani,[†] Alexander Kemper,[†] Linyou Cao,[‡] and Kenan Gundogdu*,[†]

[†]Department of Physics, North Carolina State University, Raleigh, North Carolina 27695, United States
[‡]Department of Materials Science and Engineering, North Carolina State University, Raleigh, North Carolina 27695, United States

Supporting Information

ABSTRACT: Many-body interactions in photoexcited semiconductors can bring about strongly interacting electronic states, culminating in the fully ionized matter of electron−hole plasma (EHP) and electron−hole liquid (EHL). These exotic phases exhibit unique electronic properties, such as metallic conductivity and metastable high photoexcitation density, which can be the basis for future transformative applications. However, the cryogenic condition required for its formation has limited the study of dense plasma phases to a purely academic pursuit in a restricted parameter space. This paradigm can potentially change with the recent experimental observation of these phases in atomically thin MoS_2 and $MoTe_2$ at room temperature. A fundamental understanding of EHP and EHL dynamics is critical for developing novel applications on this versatile layered platform. In this work, we studied the formation and dissipation of EHP in monolayer MoS_2. Unlike previous results in bulk semiconductors, our results reveal that electromechanical material changes in monolayer MoS_2 during photoexcitation play a significant role in dense EHP formation. Within the free-standing geometry, photoexcitation is accompanied by an unconstrained thermal expansion, resulting in a direct-to-indirect gap electronic transition at a critical lattice spacing and fluence. This dramatic altering of the material's energetic landscape extends carrier lifetimes by 2 orders of magnitude and allows the density required for EHP formation. The result is a stable dense plasma state that is sustained with modest optical photoexcitation. Our findings pave the way for novel applications based on dense plasma states in two-dimensional semiconductors.

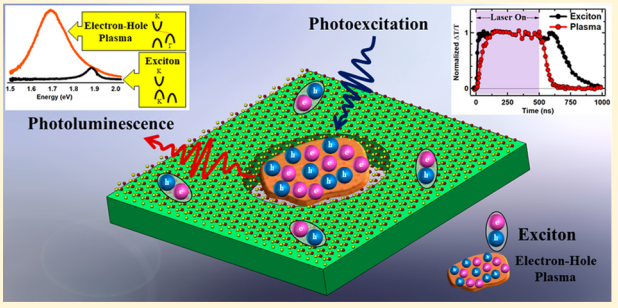

KEYWORDS: *Two-dimensional materials, MoS_2, transition metal dichalcogenides, dense electron−hole plasma, bandgap renormalization, direct to indirect bandgap transition*

The reduced dimensionality and dielectric screening for monolayer and few-layer transition metal dichalcogenides (TMDs) results in strong charge coupling and bound electron−hole pairs (excitons). For example, the binding energy between charge pairs is so strong (~0.5 eV) that excitons can exist well above room temperature.[1−3] As a result, these materials provide a new test bed for studying many-body Coulomb systems. An exciting manifestation of this is the recent discovery of Fermi liquid condensation at room temperature.[4−6] Although its existence has been known for nearly 50 years, the practical utilization of electron−hole plasma (EHP) and electron−hole liquid (EHL) has been hindered, due primarily to the cryogenic requirements for bulk semiconductors.[7] Freed from this restrictive condition, atomically thin TMDs offer the potential of EHP-based applications.

Here we report the electronic, optical, and mechanical changes during formation and dissipation of dense EHP in monolayer MoS_2. We utilized time-resolved photoluminescence and transmission to study the evolution of optical excitations between excitonic and dense plasma states and the photoexcited carrier lifetime. In addition, we used Raman spectroscopy combined with electronic band structure theory to study changes in the electronic band structure during the phase transition. Our studies reveal that the plasma phase transition in monolayer MoS_2 is a very intriguing process that involves changes in electronic band structure, recombination kinetics, and carrier lifetime. As illustrated in panels a and b of Figure 1, laser heating leads to material expansion accompanied by a direct-to-indirect gap transition. Optically excited carriers survive in the indirect gap for hundreds of nanoseconds, which promotes a high charge density and subsequent EHP formation (Figure 1c). While it is expected that the indirect gap formation should reduce the photoluminescence (PL) efficiency, we found that a small fraction of carriers that exist in the direct gap valleys radiatively recombine with a very high efficiency leading to observation of an unusual increase in the PL intensity in the EHP phase.

Received: November 1, 2018
Revised: December 21, 2018
Published: January 4, 2019

DOI: 10.1021/acs.nanolett.8b04408
Nano Lett. 2019, 19, 1104−1111

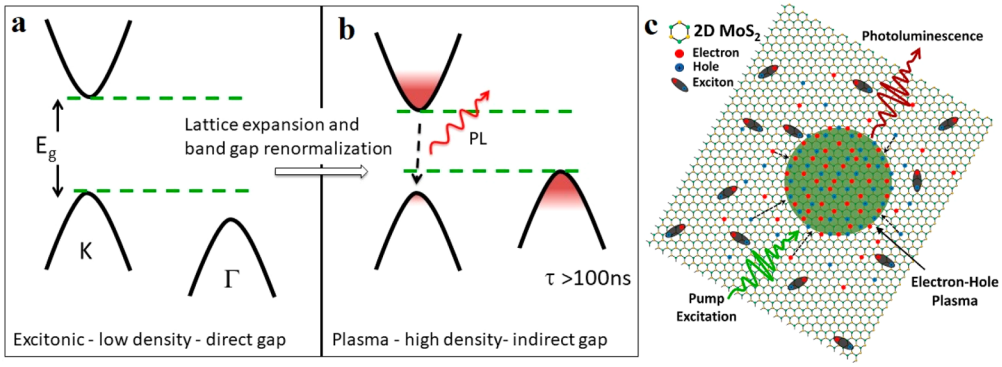

Figure 1. (a) Electronic band alignment for K and Γ valleys in MoS_2. (b) Under high photoexcitation, thermal expansion from material heating leads to an indirect bandgap formation with the conduction band minimum in the K valley and valence band maximum in the Γ valley. The long-lived (>100 ns) indirect charges allow the formation of (c) a highly ionized electron–hole plasma at room temperature.

Figure 2a shows PL spatial images under continuous-wave (CW) photoexcitation at various fluences. In this experiment, a CW laser is focused onto monolayer MoS_2 suspended over a 6 μm cavity (see Methods for sample preparation), and the resulting PL is collected using a microscope objective. As photoexcitation is increased, the PL intensity rapidly undergoes a transition from relatively weak excitonic emission to a bright, broadband, and dense EHP phase.[4,8−10] When the photoexcitation density reaches a critical value, an 18% increase in laser power results in a 540% stronger PL. Figure 2b shows the PL spectral evolution with increased photoexcitation as the phase transition takes place with high excitation fluence. At low fluence (inset of Figure 2b), the system is purely excitonic as evidenced by the linear relationship between the integrated PL and the photoexcitation (see Figure S1 for low-power spectra). As the carrier density increases, bandgap renormalization (BGR) induces a large spectral red-shift.[11] As detailed in earlier work,[4] the transition occurring at ∼3 kW cm^{-2} is ascribed to the formation of a dense plasma state at 450 K with a carrier density of $\sim 4 \times 10^{13}$ cm^{-2} (see the Supporting Information). All spectral features (width, location, and intensity) are unchanging beyond the critical intensity, indicating a constant carrier density, which could be evidence of dense plasma condensation, i.e., EHL.[7]

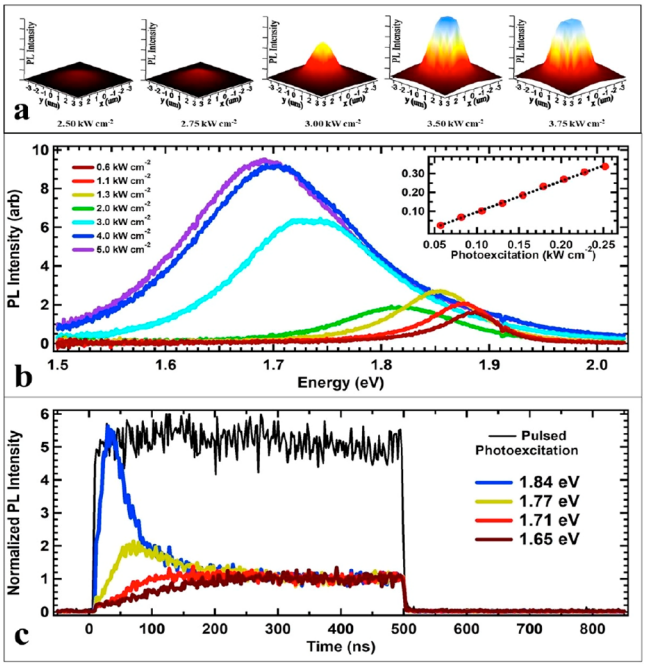

Figure 2. (a) Photoluminescence images of suspended monolayer MoS_2 under spatially uniform, steady-state photoexcitation at intensities below and above EHP formation. (b) Photoluminescence spectra measured from a 2 μm^2 area in the center of the suspended material with increasing photoexcitation. The inset shows the integrated PL vs photoexcitation at low fluence. (c) Time-resolved photoluminescence measured at different energy channels with 500 ns square-wave photoexcitation (637 nm). The photoexcitation intensity was 50% above the EHP threshold. All energy channels are normalized to the steady-state EHP intensity averaged between 300 and 500 ns. The instrument response function measured at 637 nm shows a 2 ns photoexcitation rise/fall (black curve).

The dramatic increases in PL intensity and carrier density with only a slight (18%) increase in photoexcitation suggest a phase transition accompanied by a much longer carrier lifetime. First, the increase in PL indicates a reduction in nonradiative recombination. Second, carrier recombination and photogeneration rates are balanced under steady-state excitation, i.e., dynamic equilibrium. In the limit of slow carrier diffusion, as is the case for monolayer MoS_2,[12] the dynamic equilibrium condition can be written to first order as $\frac{aI}{E} = \frac{n}{\tau}$, where a is the absorption coefficient, I is the laser intensity, E is the photon energy, n is the carrier density, and τ is the carrier lifetime. To satisfy this equality under threshold conditions (I = 3 kW cm^{-2}, a = 5%, E = 2.33 eV, and $n = 4 \times 10^{13}$ cm^{-2}), the carrier lifetime must be around 100 ns. Given the reported exciton lifetime in MoS_2 (∼1 ns),[13,14] this remarkable finding suggests a massive change in carrier behavior exemplified by a lifetime that is 2 orders of magnitude longer.

To study EHP formation, we first characterized the carrier lifetime using time-resolved PL experiments (trPL) via time-correlated single-photon counting. Figure 2c shows PL evolution at four different photon energies when the material is excited using 500 ns square-wave laser pulses at 637 nm with an intensity 50% above the EHP threshold for CW conditions (3 mW). Upon photoexcitation, fast-rising emission associated with exciton recombination (1.84 eV in Figure 2c) dominates the spectrum. The excitonic emission then transfers spectral weight to the broadband EHP state (1.65 eV in Figure 2c) in ∼100 ns. The PL reaches a steady-state condition at ∼300 ns; i.e., the spectrum is unchanging. Surprisingly, once photoexcitation ceases at 500 ns, the PL is extinguished within the

DOI: 10.1021/acs.nanolett.8b04408
Nano Lett. 2019, 19, 1104−1111

experimental resolution (<2 ns) for all measured photon energies. The immediate disappearance of the PL appears to contradict the spectrally derived carrier density due to the apparent short PL lifetime. In other words, either the carrier density is grossly overestimated or long-lived carriers cease to radiatively recombine after photoexcitation stops.

To investigate the potential reasons behind the sudden disappearance of the emission during the trPL experiment, we studied changes in the material's electronic band structure using a combination of experimental Raman spectroscopy and theoretical electronic band structure calculations. Raman spectroscopy measures strain and temperature due to lattice expansion and laser heating, respectively. For monolayer MoS_2, the in-plane E′ and out-of-plane A_1 Raman modes are sensitive to lattice spacing, where the former is primarily used to infer strain.[15,16] These modes are shown in panels a and b of Figure 3 for both anti-Stokes and Stokes scattering as a function of photoexcitation. Two important trends are observed with increasing photoexcitation: (1) a spectral red-shifting and (2) a relative increase in the anti-Stokes intensity. A Lorentzian profile is fit to the E′ mode whose peak position is plotted versus laser intensity in Figure 3c. Using the calibrated results of Lloyd et al.,[17] the peak position is converted to a lattice expansion. The material is found to have a positive prestrain with no photoexcitation, which is likely a result of the transfer process. The material temperature is obtained by comparing the Stokes and anti-Stokes intensity ratio through a Boltzmann factor (see the Supporting Information) and is plotted in Figure 3c. The shaded regions in Figure 3c represent the exciton and EHP phases as determined by the PL spectrum. Raman analysis at the EHP threshold indicates a material temperature of ∼425 K accompanied by a lattice expansion of ∼1.25% from photothermal expansion. We note that the measured lattice temperature using this Raman method matches our earlier result obtained using PL analysis.[4]

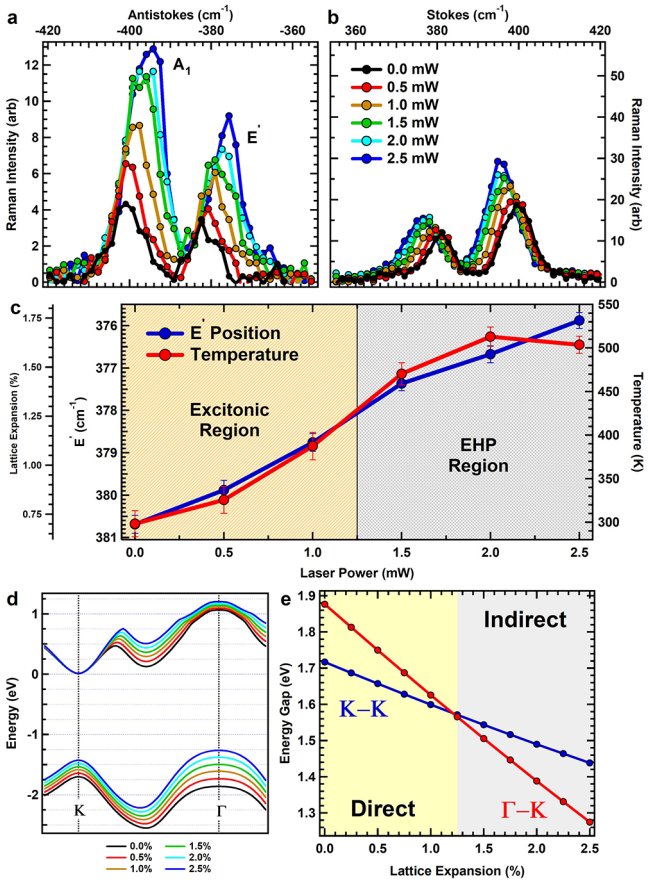

Figure 3. Raman spectrum for (a) anti-Stokes and (b) Stokes scattering as a function of 637 nm photoexcitation. (c) Power dependence of the lattice temperature (right axis) and expansion (left axes) determined by Raman anti-Stokes to Stokes ratio and E′ peak position analysis, respectively. (d) Calculated electronic band structure from density functional theory calculations for different lattice expansion values. (e) Calculated bandgap energy for direct (K−K, blue curve) and indirect (Γ−K, red curve) valleys.

Experiments and density functional theory (DFT) calculations show strain, or in our case thermal expansion, has a significant impact on the material's electronic band structure, including a direct-to-indirect transition.[18−20] Figure 3d shows the evolution of the calculated electronic band structure as a function of biaxial lattice expansion. As the lattice ions move farther apart, the energy of the indirect Γ valley increases relative to that of the direct K valley. Via comparisonn of the K−K and Γ−K energy gaps plotted in Figure 3e, a direct-to-indirect transition is expected for an expansion of 1.25%, thus showing a strong correlation with the onset of EHP formation (see Figure 3c). Fully formed EHP (∼1.75% expansion) shows a sizable indirectness as the Γ−K energy gap is ∼70 meV lower than the K−K energy gap. Therefore, the EHP state in monolayer MoS_2 is found in a material with an indirect bandgap. Carrier recombination for an indirect gap semiconductor is mostly nonradiative and thus absent in the trPL for times after photoexcitation. The situation during continuous photoexcitation is similar, except carriers are created within the direct bandgap and can contribute to the PL prior to scattering into the lower-energy indirect valleys.

Because the material becomes an indirect gap semiconductor, the PL experiments are not effective in measuring the carrier population that is potentially surviving in the indirect bands. We measured the population of these "dark" carriers and their dynamics using differential transmission spectroscopy. This experiment measures the change in broadband optical transmission ("probe") due to sample photoexcitation ("pump"). The pump pulse excites the sample and drives the system from excitonic to dense plasma states. The relative transmission of the probe pulse changes with respect to the unexcited sample. Because transmission depends on the availability of states, this experiment is sensitive to carrier populations regardless of whether they can radiatively recombine. Figure 4a shows the differential transmission's spectral evolution for MoS_2 driven to EHP. Spectral line-outs shown in panels b and c of Figure 4 reveal four distinct features and are attributed to bound and unbounded ("free") charge states. The two features at 1.90 and 2.04 eV are the A and B excitons, respectively.[21−23] These excitonic transitions are situated entirely within the K valley and are energy-separated by spin−orbit coupling.[24] Because excitonic transitions are photobleached at a high carrier density, the intensity of the differential transmission signal increases at these spectral positions.[23] The negative transmission signal below 1.85 eV and above 2.15 eV arises from the conduction band red-shift due to the high density of free charges, i.e., bandgap renormalization.[25−27] In other words, closing of the electronic bandgap due to BGR opens more absorption pathways at lower energies relative to the unexcited material, which results in a transmission decrease below 1.85 eV. The same effect

DOI: 10.1021/acs.nanolett.8b04408
Nano Lett. 2019, 19, 1104−1111

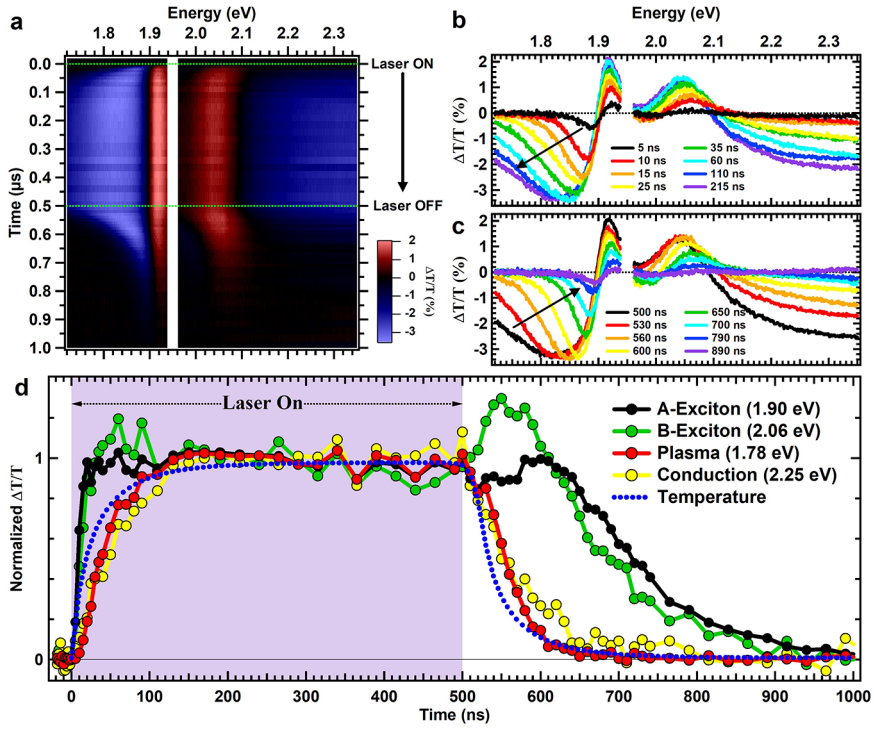

Figure 4. (a) Time-resolved differential transmission spectrum with 500 ns square-wave photoexcitation (green dashed lines). Spectral line-outs at various times during (b) EHP formation and (c) decay. (d) Temporal line-outs are shown at A (black) and B (green) exciton energies and at energies corresponding to dense plasma (red) and conduction band (yellow) states affected by bandgap renormalization. The temperature (blue dashed) dynamics for the material center is shown alongside the differential transmission. All energy channels are normalized to the steady-state EHP intensity averaged between 300 and 500 ns.

causes increased absorption above 2.15 eV due to the monotonically increasing absorption with respect to energy.

Figure 4d shows the temporal evolution corresponding to each of the excited species. To visualize the contrast between time evolutions of each species, we plot the absolute value of $\Delta T/T$. All spectral features grow with the onset of laser excitation until a saturation is reached at ∼200 ns. Likewise, signal decay begins once photoexcitation ceases at 500 ns, after which all signals eventually relax back to zero. All curves are normalized to the average EHP-state value (300−500 ns). The temporal line-outs in Figure 4d show a significant difference in the growth and decay time scales between excitonic and free charge states, the former rising nearly as fast as the photoexcitation (<10 ns) and the latter in >100 ns. Because most exciton recombination and other microscopic processes in monolayer MoS_2 occur on subnanosecond time scales, we consider changes in lattice temperature as the primary cause for the slow rise and fall in the free charge states. This conclusion is further supported by comparing temperature dynamics calculated from a simplified heat diffusion model with the free charge dynamics in Figure 4d (see the Supporting Information). Therefore, the growth of dense plasma coincides with photothermal expansion and the transition to an indirect bandgap. More importantly, charge carriers remain in the material long after photoexcitation has ceased and much longer than the direct valley exciton lifetime (<10 ns).[13]

Both the differential transmission and the Raman experiments indicate that electrons and holes mostly occupy an indirect gap when EHP is reached. Generally, radiative recombination is suppressed for an indirect gap semiconductor. Thus, our experiments should show a decrease in PL emission when the direct-to-indirect transition occurs. However, the steady-state PL measurement in panels a and b of Figure 2 shows the PL emission intensity increasing >5-fold at the EHP threshold. It appears that while most of the carriers occupy an indirect valley, the carriers that radiatively recombine in the direct valley do so with a surprisingly high efficiency. In the CW PL measurements (Figure 2a,b), a fraction of the carriers will always occupy the direct gap because the (continuous) photoexcitation originates in the direct K−K band.

To further reveal the long-lived "dark" carriers, we performed an additional trPL experiment. We photoexcite the system to the EHP phase in the same manner described previously (cf. Figure 2c), but an additional CW "probe" laser at 532 nm is added to this experiment and focused to the same spatial location as the photoexcitation laser. The sole function of the probe laser is to add a continuous "trickle" of charges into the direct bandgap. Although many of these additional carriers will scatter into the indirect gap, some will radiatively recombine in the direct gap, thereby revealing the spectral evolution of the system's energy levels. The probe power was 10-fold lower than the pulsed photoexcitation to prevent any significant perturbation to the EHP formation and decay process. Indeed, the PL dynamics with the added CW laser (Figure 5a) have very similar formation dynamics for the case of no CW excitation (Figure 2c). Unlike Figure 2c, there are significant deviations in the trPL signal after photoexcitation (>500 ns), which supports the long-lived charge carrier observation in the transmission experiment.

Figure 5b reveals the PL time evolution at different spectral positions after the pump pulse has ceased. The low energy emission that we associate with EHP (1.65 eV) persists for >150 ns after pump extinction without photoexcitation.

DOI: 10.1021/acs.nanolett.8b04408
Nano Lett. 2019, 19, 1104−1111

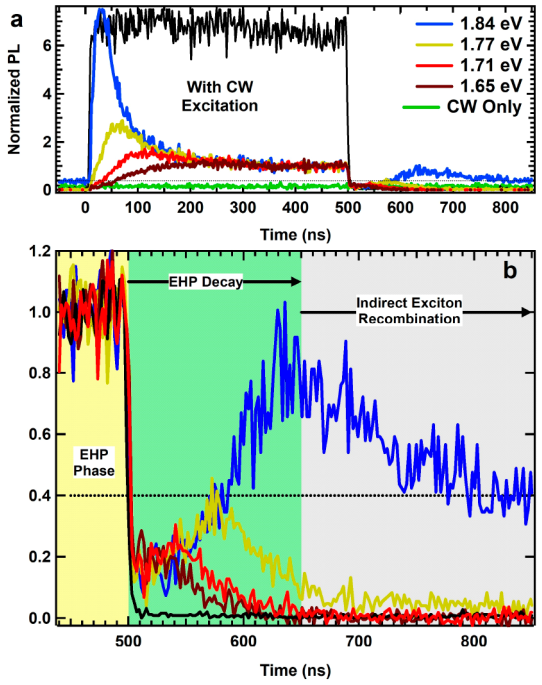

Figure 5. (a) Time-resolved photoluminescence measured at different energy channels with 500 ns square-wave photoexcitation (637 nm) and CW photoexcitation (532 nm). The 637 nm photoexcitation intensity was 50% above the EHP threshold (3 mW), and the 532 nm photoexcitation was 10 times weaker (0.3 mW). All energy channels are normalized to the steady-state EHP intensity averaged between 300 and 500 ns. Photoluminescence at the exciton energy channel (1.84 eV) with CW-only photoexcitation is shown as the green curve. The instrument response function measured at 637 nm shows a 2 ns photoexcitation rise/fall (black curve). Once excited to EHP, the overall exciton energy channel (blue) is offset by a factor of ~2 (black dashed). (b) Photoluminescence after pulsed photoexcitation showing EHP decay dynamics and long-lived charge lifetime.

Coinciding with the EHP decay, the excitonic emission (1.84 eV) increases for 150 ns, which is consistent with thermal contraction and reduced BGR. At 650 ns, the spectral shift ends and the PL emission is dominated by exciton recombination, which eventually decays in >300 ns. Remarkably, the brightness of the exciton emission at 650 ns is double the long time, no photoexcitation value (black dashed vs blue curve in Figure 5b). If the only carriers in the material are created by the CW probe laser, then the PL emission should not rise above the equilibrium value and should decrease due to the elevated temperature and strain.[28,29] Therefore, this observation must be linked to the presence of long-lived indirect carriers.

It should be noted that the excitonic PL is higher for $t < 0$ compared to CW-only (blue and green curves in Figure 5a) excitation. Therefore, driving the system to EHP has a long-term effect (>200 μs given the 5 kHz repetition rate) on the material in the form of a higher PL efficiency. A possible mechanism is through the temporary p-doping of sulfur vacancies made available from the free charge states at high excitation. Although previous studies have shown similar photodoping effects,[30,31] the question of whether it is present in this system remains open.

The optical diagnostics employed in this study not only paint a picture of the changing energetic landscape when monolayer MoS_2 is driven to EHP formation, they also indicate that the observed changes are unlikely due to defect states. First, the results are reproducible across numerous samples and with multiple power sweeps on the same material. If the PL transition was due to defect formation at high photoexcitation, we should not observe a threshold behavior in the second or later power sweeps. Instead, we observe a consistent threshold behavior for every power sweep across all measured suspended monolayers. Second, the Raman and low-power PL spectrum undergoes almost no change after photoexcitation.[4] Furthermore, none of the reported defects in the scientific literature fully match the PL trends reported in this work in spectrum, temperature, and photoexcitation. Commonly reported defect states in MoS_2 originate from sulfur vacancies,[32,33] oxygen treatment,[34] bright edge states,[35,36] and laser cleaning.[37] However, we can generally exclude these defects as a cause

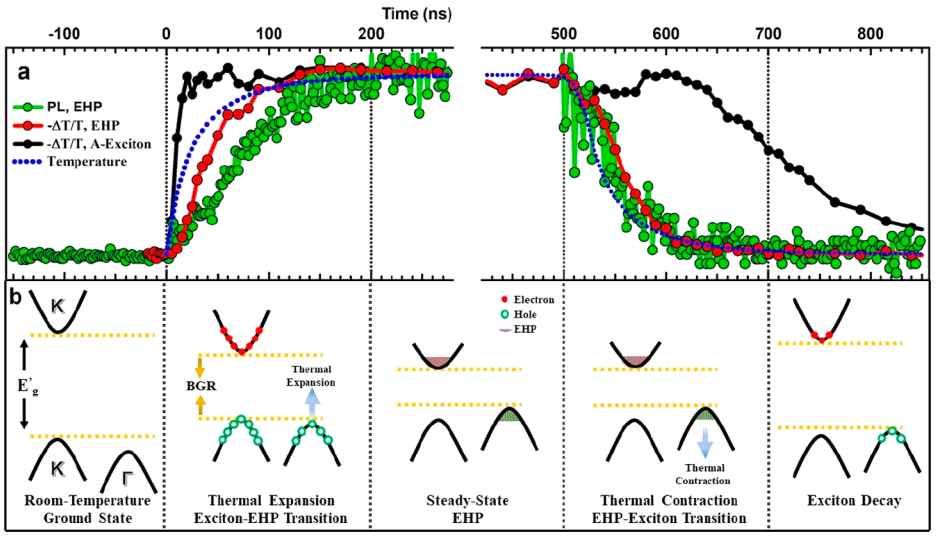

Figure 6. (a) Summary of optical dynamics. EHP response shown by time-resolved photoluminescence at 1.65 eV (green) and time-resolved differential transmission at 1.78 eV (red), excitonic response at 1.90 eV (black), and temperature dynamics from a heat diffusion model (blue dashed). All curves are normalized to the steady-state EHP condition averaged between 300 and 500 ns. (b) Electronic band diagram depicted at all phases of EHP formation and decay.

DOI: 10.1021/acs.nanolett.8b04408
Nano Lett. 2019, 19, 1104−1111

for the anomalous PL increase due to the phenomenon's reversibility and negligible material change. Specifically, sulfur vacancy emission is most prominent at low temperature, which is unlike the dramatic PL increase at elevated temperature in this system. Monolayer MoS_2 treated with oxygen plasma shows PL quenching with an increased level of exposure and little change in the spectral line shape.[34] Although bright edge states formed by oxygen annealing show a large PL enhancement, it is only observed at the exciton peak (1.85 eV) with no significant spectral broadening.[35,36] Lastly, the process of laser cleaning at elevated photoexcitation requires treatment for minutes and produces a narrow excitonic PL,[37] rather than the broadband and near-instantaneous spectrum reported here.

The diagram presented in Figure 6b illustrates the changes in the material's band structure and charge population dynamics, separated into five distinct steps. The material begins its journey ($t < 0$) in the electronic ground state (no free charges), at room temperature (293 K), and has a direct bandgap (K−K). Laser excitation beginning at $t = 0$ provokes an immediate growth in exciton density (K−K), which is accompanied by BGR. The dynamic equilibrium of the excitons is soon established (10−20 ns), where charge creation and annihilation are in balance. The majority of absorbed light is converted into heat, as nonradiative recombination dominates monolayer MoS_2 under these conditions.[13] The resulting temperature increase causes the material to undergo thermal expansion (0 ns < t < 200 ns) and lifts the valence Γ band above the K band. As the direct-to-indirect transition continues, charges are transferred into the Γ valley whose extended lifetime precipitates the high charge density and stability required for EHP formation. The system maintains EHP for as long as photoexcitation and laser heating are supplied (500 ns in our case). The cessation of photoexcitation at t = 500 ns begins the system's relaxation phase that is defined by material cooling, lattice contraction, and charge recombination. The fact that EHP persists for >50 ns without photoexcitation and shows no trace of radiative recombination suggests it resides entirely within the Γ valley. The excitation cycle ends with a slow decay phase (∼1 μs) defined by indirect exciton recombination occurring after EHP has died off and the material has cooled back to room temperature (∼700 ns).

The surprising observation of enhanced photoluminescence accompanying a direct-to-indirect bandgap transition highlights a long-standing topic within the field of dense semiconductor plasma. Nonradiative pathways, i.e., Auger recombination, should be enhanced at a higher charge density and lead to shorter lifetimes; thus, contrary to our results, one would expect a reduced PL. However, earlier studies of carrier recombination dynamics show that in optically excited Fermi degenerate indirect bandgap semiconductors, normal Auger recombination is highly suppressed due to energy and momentum conservation.[38] As a result, a dense plasma state can exhibit both an increased lifetime and a high carrier density, both of which are observed in our experiments. The EHP in our study does indeed satisfy the Fermi degenerate condition, $T_F/T = n\pi\hbar^2/mkT \simeq 6 > 1$, where a factor of 2 for spin has been included. We believe our results will help stimulate further theoretical and experimental efforts in the investigation of photoexcitation dynamics under degenerate conditions in two-dimensional materials.

The energetic roller coaster driving room-temperature EHP points toward a rich, dynamic system whose material properties can be tuned and reset at MHz frequencies. It remains to be seen just how long EHP can persist in monolayer TMDs after photoexcitation has ended, using the appropriate lattice conditions, material combination, and photoexcitation scheme. The understanding of dynamic electronic structure and its effects on charge excitation will guide future efforts in generating and manipulating high-carrier density electronic states using ultrafast photoexcitation, and will help in engineering favorable geometries for high-power optoelectronic devices.

Methods. *Sample Preparation.* Complete details of the growth and transfer process can be found in ref 4. Briefly, CVD-grown monolayer MoS_2 was transferred onto a chemically etched quartz substrate. The quartz substrate was patterned with an array of 6 μm diameter cavities using photolithography and dry etching. The transfer process entailed dissolving polystyrene in toluene, followed by spin-coating on the as-grown monolayer, followed by baking for 1 h at 80−90 °C. A water droplet was placed on the polystyrene−monolayer assembly for substrate delamination, after which the monolayer was transferred to the quartz substrate. This was followed by another a 1 h bake and removal of the polystyrene with a toluene rinse. All measurements were performed under vacuum conditions (30 mTorr).

CW Photoluminescence. CW photoluminescence was performed using a 532 nm TEM00 diode laser (Verdi, Coherent) focused 45° relative to the sample's surface. The measured spot size at the sample's surface was 35 μm [full width at half-maximum (fwhm)], thus providing a near-uniform intensity profile across the 6 μm suspension. Photoluminescence was collected by a 50× microscope objective and sent through a 570 nm long-pass filter. The photoluminescence was imaged onto the entrance slit of a spectrometer (Acton) using a 2× tube lens for a total of 100× magnification. Spatial−spatial (Figure 1a) and spatial−spectral images were recorded using a deep-cooled CCD instrument (PIXIS, Princeton Instruments). Spectra in Figure 1b were extracted from the spatial−spectral images in a 2 μm^2 area located at the center of the suspended region. See Figure S6 for the experimental diagram.

Time-Resolved Photoluminescence. Time-resolved photoluminescence (trPL) was photoexcited using a 637 nm TEM00 diode laser (OBIS, Coherent) focused through a 50× microscope objective to a 1.6 μm spot size (fwhm) in the center of the suspended region. The laser was triggered on and off using TTL pulses from a delay generator (DG535, Stanford Research Systems). The resulting laser pulse was a square wave with a 2 ns rise, a 500 ns on time, and a 2 ns fall and was repeated at 50 kHz (2.5% duty cycle). Photoluminescence was collected by the same 50× microscope objective and passed through a 638 nm notch filter. The photoluminescence wavelength was selected using a monochromator (5 nm bandwidth) and then detected using a PMT instrument (H10721-20, Hamamatsu). The temporal resolution was obtained by sending timing signals from the delay generator ("start") and PMT instrument ("stop") to a custom-built time-correlated single-photon counting (TCSPC) system. Although the TCSPC resolution was 200 ps, the experimental timing was ultimately limited to 2 ns determined by the laser rise/fall time. See Figure S7 for the experimental diagram.

Raman Spectroscopy. Raman spectroscopy was performed using the same photoexcitation laser (637 nm) as the trPL, although operated in CW mode. The 532 nm Raman laser

DOI: 10.1021/acs.nanolett.8b04408
Nano Lett. 2019, 19, 1104−1111

(Verdi, Coherent) was focused by a 50× microscope objective to a 1.6 μm spot size (fwhm) using a colinear geometry. The Raman signal was collected by the same imaging system as the CW photoluminescence experiment. A 533 nm notch filter (Thorlabs) with a 17 nm bandwidth was used to filter the fundamental laser frequency and obtain both Stokes and anti-Stokes peaks; 0.3 mW of Raman laser power for 120 s of exposure was used for all Raman versus photoexcitation measurements.

Electronic Band Structure Theory. The electronic structure and phonon calculations were performed using DFT as implemented in the open source code Quantum ESPRESSO.[39] We used plane-wave, fully relativistic pseudopotentials with nonlinear core correction. The exchange-correlation energy was described by the generalized gradient approximation (GGA), in the scheme proposed by Perdew, Burke, and Ernzerhof intended for solid-state and surface systems (PBEsol).[40] The cutoff energy used was 70 Ry. The Brillouin zone (BZ) was sampled for integrations according to the scheme proposed by Monkhorst and Pack[41] with a grid of 14 × 14 × 1 k-points. The out-of-plane lattice constant c was set at 25 Å in a slab geometry to consider the monolayer system. The in-plane lattice parameter was determined by minimization of the total energy for the monolayers and was found to be 3.1492 Å. A biaxial tensile strain was introduced by varying the in-plane lattice constant a. For each strain/lattice expansion, the z coordinates of the chalcogen atoms were optimized and subsequently the electronic structure was calculated. The phonon frequencies were evaluated for each strain/lattice expansion at the Γ point. The variation of the Raman-active in-plane E′ and out-of-plane A_1 modes was evaluated for comparison to the Raman spectroscopy measurements.

Time-Resolved Differential Transmission. Time-resolved differential transmission was performed using the same photoexcitation laser (637 nm) and pulse width (500 ns) that were used in the trPL experiment. White light from an optical parametric amplifier (OPA 9400, Coherent) pumped by an amplified femtosecond laser (RegA 9000, Coherent) was used as the transmission ("probe") signal. The probe light (200 fs pulses at a 10 kHz repetition rate) was focused by a 50× microscope objective to a 1.6 μm spot size (fwhm) using a colinear geometry with respect to the photoexcitation laser. After passing through the sample and exiting the vacuum chamber, the probe light was collected by a 50× microscope objective and imaged onto the entrance slit of an integrated CCD spectrometer (Fergie, Princeton Instruments). Operating in kinetics spectroscopy mode, the Fergie was electronically triggered by the 10 kHz RegA source, thus acquiring each probe pulse. Externally triggered by the RegA source, a DG535 triggered the photoexcitation laser at 5 kHz with an adjustable time delay relative to the probe light. The output from this configuration was a 10 kHz probe (white light, 200 fs) with a 5 kHz photoexcitation (637 nm, 500 ns) with phase adjustability provided by the DG535 instrument. For each time step, alternating probe and pump+probe spectra from the Fergie were recorded and then processed to give $\Delta T/T$. Time sweeping was provided by the DG535 instrument by adjusting the relative time between the pump and probe. Every time step in Figure 3a is averaged over ∼750 $\Delta T/T$ spectra. Although the timing system was capable of 20 ps resolution, the experimental timing was limited by the laser rise/fall time (2 ns). See Figure S8 for the experimental diagram.

■ ASSOCIATED CONTENT

Supporting Information

The Supporting Information is available free of charge on the ACS Publications website at DOI: 10.1021/acs.nanolett.8b04408.

Low-power photoluminescence evolution, reproducibility, charge density measurement from bandgap renormalization (BGR), material temperature from Raman analysis, heat diffusion model, experimental diagrams, and additional references (PDF)

■ AUTHOR INFORMATION

Corresponding Author

*E-mail: kenan_gundogdu@ncsu.edu.

ORCID

Avinash Rustagi: 0000-0001-6776-9496
Alexander Kemper: 0000-0002-5426-5181
Linyou Cao: 0000-0002-7834-8336
Kenan Gundogdu: 0000-0001-7149-5766

Author Contributions

K.G., A.W.B., and R.A.Y. designed the research. L.C. and Y.Y. provided the samples. A.W.B. and R.A.Y. performed the optical and Raman measurements and analyzed the experimental data. A.K. and A.R. performed the theoretical calculations. A.W.B. drafted the manuscript with K.G. and received contributions from all authors.

Notes

The authors declare no competing financial interest.

■ ACKNOWLEDGMENTS

The authors acknowledge funding from the United States Army Research Office Grant W911NF-17-1-0483 and the National Science Foundation Grant DMR-1709934 and the OBIS laser gift from Coherent Lasers.

■ REFERENCES

(1) Feng, J.; Qian, X.; Huang, C.-W.; Li, J. *Nat. Photonics* **2012**, *6* (12), 866.
(2) Klots, A.; Newaz, A.; Wang, B.; Prasai, D.; Krzyzanowska, H.; Lin, J.; Caudel, D.; Ghimire, N.; Yan, J.; Ivanov, B.; et al. *Sci. Rep.* **2015**, *4*, 6608.
(3) Yu, Y.; Yu, Y.; Cai, Y.; Li, W.; Gurarslan, A.; Peelaers, H.; Aspnes, D. E.; Van de Walle, C. G.; Nguyen, N. V.; Zhang, Y.-W.; Cao, L. *Sci. Rep.* **2015**, *5*, 16996.
(4) Yu, Y.; Bataller, A.; Younts, R.; Yu, Y.; Li, G.; Puretzky, A. A.; Geohegan, D. B.; Gundogdu, K.; Cao, L. *arXiv* **2017**, 1710.09538.
(5) Rustagi, A.; Kemper, A. F. *Nano Lett.* **2018**, *18* (1), 455−459.
(6) Arp, T. B.; Pleskot, D.; Aji, V.; Gabor, N. M. *arXiv* **2017**, 1711.06917.
(7) Jeffries, C. D.; Keldysh, L. u. d. V. *Electron-Hole Droplets in Semiconductors*; North Holland, 1983; Vol. *6*.
(8) Pokrovskii, Y. E.; Svistunova, K. *ZhETF Pisma Redaktsiiu* **1969**, *9*, 435.
(9) Smith, L.; Wolfe, J. *Phys. Rev. B: Condens. Matter Mater. Phys.* **1995**, *51* (12), 7521.
(10) Shimano, R.; Nagai, M.; Horiuch, K.; Kuwata-Gonokami, M. *Phys. Rev. Lett.* **2002**, *88* (5), 057404.
(11) Tränkle, G.; Lach, E.; Forchel, A.; Ell, C.; Haug, H.; Weimann, G.; Griffiths, G.; Kroemer, H.; Subbanna, S. *J. Phys., Colloq.* **1987**, *48* (C5), C5-385−C5-388.
(12) Radisavljevic, B.; Radenovic, A.; Brivio, J.; Giacometti, i. V.; Kis, A. *Nat. Nanotechnol.* **2011**, *6* (3), 147.

DOI: 10.1021/acs.nanolett.8b04408
Nano Lett. 2019, 19, 1104−1111

(13) Amani, M.; Lien, D.-H.; Kiriya, D.; Xiao, J.; Azcatl, A.; Noh, J.; Madhvapathy, S. R.; Addou, R.; Santosh, K.; Dubey, M.; et al. *Science* **2015**, *350* (6264), 1065−1068.
(14) Yu, Y.; Yu, Y.; Xu, C.; Barrette, A.; Gundogdu, K.; Cao, L. *Phys. Rev. B: Condens. Matter Mater. Phys.* **2016**, *93* (20), 201111.
(15) Chakraborty, B.; Bera, A.; Muthu, D. V. S.; Bhowmick, S.; Waghmare, U. V.; Sood, A. K. *Phys. Rev. B: Condens. Matter Mater. Phys.* **2012**, *85* (16), 161403.
(16) Rice, C.; Young, R. J.; Zan, R.; Bangert, U.; Wolverson, D.; Georgiou, T.; Jalil, R.; Novoselov, K. S. *Phys. Rev. B: Condens. Matter Mater. Phys.* **2013**, *87* (8), 081307.
(17) Lloyd, D.; Liu, X.; Christopher, J. W.; Cantley, L.; Wadehra, A.; Kim, B. L.; Goldberg, B. B.; Swan, A. K.; Bunch, J. S. *Nano Lett.* **2016**, *16* (9), 5836−41.
(18) Lu, P.; Wu, X.; Guo, W.; Zeng, X. C. *Phys. Chem. Chem. Phys.* **2012**, *14* (37), 13035−40.
(19) Pan, H.; Zhang, Y.-W. *J. Phys. Chem. C* **2012**, *116* (21), 11752−11757.
(20) Conley, H. J.; Wang, B.; Ziegler, J. I.; Haglund, R. F., Jr.; Pantelides, S. T.; Bolotin, K. I. *Nano Lett.* **2013**, *13* (8), 3626−30.
(21) Mak, K. F.; Lee, C.; Hone, J.; Shan, J.; Heinz, T. F. *Phys. Rev. Lett.* **2010**, *105* (13), 136805.
(22) Shi, H.; Yan, R.; Bertolazzi, S.; Brivio, J.; Gao, B.; Kis, A.; Jena, D.; Xing, H. G.; Huang, L. *ACS Nano* **2013**, *7* (2), 1072−1080.
(23) Mai, C.; Barrette, A.; Yu, Y.; Semenov, Y. G.; Kim, K. W.; Cao, L.; Gundogdu, K. *Nano Lett.* **2014**, *14* (1), 202−6.
(24) Zhu, Z. Y.; Cheng, Y. C.; Schwingenschlögl, U. *Phys. Rev. B: Condens. Matter Mater. Phys.* **2011**, *84* (15), 153402.
(25) Pogna, E. A.; Marsili, M.; De Fazio, D.; Dal Conte, S.; Manzoni, C.; Sangalli, D.; Yoon, D.; Lombardo, A.; Ferrari, A. C.; Marini, A.; Cerullo, G.; Prezzi, D. *ACS Nano* **2016**, *10* (1), 1182−8.
(26) Chernikov, A.; Ruppert, C.; Hill, H. M.; Rigosi, A. F.; Heinz, T. F. *Nat. Photonics* **2015**, *9* (7), 466−470.
(27) Sie, E. J.; Frenzel, A. J.; Lee, Y.-H.; Kong, J.; Gedik, N. *Phys. Rev. B: Condens. Matter Mater. Phys.* **2015**, *92* (12), 125417.
(28) Korn, T.; Heydrich, S.; Hirmer, M.; Schmutzler, J.; Schüller, C. *Appl. Phys. Lett.* **2011**, *99* (10), 102109.
(29) Tongay, S.; Zhou, J.; Ataca, C.; Lo, K.; Matthews, T. S.; Li, J.; Grossman, J. C.; Wu, J. *Nano Lett.* **2012**, *12* (11), 5576−80.
(30) Wang, X. H.; Ning, J. Q.; Su, Z. C.; Zheng, C. C.; Zhu, B. R.; Xie, L.; Wu, H. S.; Xu, S. J. *RSC Adv.* **2016**, *6* (33), 27677−27681.
(31) He, Z.; Wang, X.; Xu, W.; Zhou, Y.; Sheng, Y.; Rong, Y.; Smith, J. M.; Warner, J. H. *ACS Nano* **2016**, *10* (6), 5847−55.
(32) Najmaei, S.; Yuan, J.; Zhang, J.; Ajayan, P.; Lou, J. *Acc. Chem. Res.* **2015**, *48* (1), 31−40.
(33) Tongay, S.; Suh, J.; Ataca, C.; Fan, W.; Luce, A.; Kang, J. S.; Liu, J.; Ko, C.; Raghunathanan, R.; Zhou, J.; et al. *Sci. Rep.* **2013**, *3*, 2657.
(34) Kang, N.; Paudel, H. P.; Leuenberger, M. N.; Tetard, L.; Khondaker, S. I. *J. Phys. Chem. C* **2014**, *118* (36), 21258−21263.
(35) Nan, H.; Wang, Z.; Wang, W.; Liang, Z.; Lu, Y.; Chen, Q.; He, D.; Tan, P.; Miao, F.; Wang, X.; Wang, J.; Ni, Z. *ACS Nano* **2014**, *8* (6), 5738−5745.
(36) Gutiérrez, H. R.; Perea-López, N.; Elías, A. L.; Berkdemir, A.; Wang, B.; Lv, R.; López-Urías, F.; Crespi, V. H.; Terrones, H.; Terrones, M. *Nano Lett.* **2013**, *13* (8), 3447−3454.
(37) He, Z.; Wang, X.; Xu, W.; Zhou, Y.; Sheng, Y.; Rong, Y.; Smith, J. M.; Warner, J. H. *ACS Nano* **2016**, *10* (6), 5847−5855.
(38) Haug, A. *Solid State Commun.* **1977**, *22* (8), 537−539.
(39) Giannozzi, P.; Baroni, S.; Bonini, N.; Calandra, M.; Car, R.; Cavazzoni, C.; Ceresoli, D.; Chiarotti, G. L.; Cococcioni, M.; Dabo, I.; et al. *J. Phys.: Condens. Matter* **2009**, *21* (39), 395502.
(40) Perdew, J. P.; Ruzsinszky, A.; Csonka, G. I.; Vydrov, O. A.; Scuseria, G. E.; Constantin, L. A.; Zhou, X.; Burke, K. *Phys. Rev. Lett.* **2008**, *100* (13), 136406.
(41) Monkhorst, H. J.; Pack, J. D. *Phys. Rev. B* **1976**, *13* (12), 5188.

DOI: 10.1021/acs.nanolett.8b04408
Nano Lett. 2019, 19, 1104−1111